JOURNAL OF GEOPHYSICAL RESEARCH, VOL. 112, C03021, doi:10.1029/2006JC003551, 2007

Statistical and dynamical analyses of generation mechanisms of solitary internal waves in the northern South China Sea

Quanan Zheng,[1] R. Dwi Susanto,[2] Chung-Ru Ho,[3] Y. Tony Song,[4] and Qing Xu[1]

Received 15 February 2006; revised 24 October 2006; accepted 20 November 2006; published 30 March 2007.

[1] This study analyzes the effects of thermocline shoaling on the ocean internal wave (IW) generation in the north South China Sea (NSCS). Seven years of satellite synthetic aperture radar (SAR) images from 1995 to 2001 are used for the statistical analysis of IW occurrence, and field measurements of sea surface wind, sea state, and vertical temperature profiles are used for analyzing IW generation and SAR imaging conditions. Latitudinal distribution of IW packets shows that 22% of IW packets distributed in the east of 118°E obviously originate from the Luzon Strait, and 78% of IW packets west of 118°E may propagate from the east or evolve into the solitons originating from the east boundary owing to the fission effect of shoaling thermocline. The yearly distribution of IW occurrence frequencies reveals an interannual variability, implying that there are long-term and large-scale processes modifying the SAR-observed IW occurrence. The monthly SAR-observed IW occurrence frequencies show that the high frequencies are distributed from April to July and reach a peak in June with a maximum frequency of 20%. The low occurrence frequencies are distributed in winter from December to February of next year with a minimum frequency of 1.5% in February. This study proposes that the IW generation needs the necessary and sufficient conditions: initial disturbance formation and wave amplitude growth. Owing to the dissipation effect on the initial disturbance, only fully grown waves have a chance to radiate out of the source region. A physical model and PKdV equation are adopted for analyzing the sufficient conditions for solitary IW amplitude growth. The results indicate that the thermocline shoaling provides the forcing to soliton amplitude growth, so that the soliton amplitude growth ratio (SAGR) serves as a decisive factor for the IW occurrence frequency. Theoretical analysis predicts a linear relation between the two. Application of theoretical models to field measurements in the Luzon Strait gives a correlation coefficient as high as 0.845 with a confidence level of 99% for months from March to November. The linear regression gives a correlation coefficient (R^2) of 0.6519 and a SAGR threshold (minimum) value of 0.90 for IW occurrence. According to the theoretical solutions, the eastward propagating disturbances have no chance to grow up, so that they hardly appear on the east side of the submarine ridges in the eastern Luzon Strait.

Citation: Zheng, Q., R. D. Susanto, C.-R. Ho, Y. T. Song, and Q. Xu (2007), Statistical and dynamical analyses of generation mechanisms of solitary internal waves in the northern South China Sea, *J. Geophys. Res.*, *112*, C03021, doi:10.1029/2006JC003551.

1. Introduction

[2] Satellite sensor imaging and field observations have revealed that the northern South China Sea, around from 19°N to 22°N latitude and from 114°E to 122°E longitude, is an ocean area where the energetic internal waves occur frequently [*Liu et al.*, 1998; *Hsu and Liu*, 2000; *Zhao et al.*, 2004; *Liu et al.*, 2004]. Satellite SAR images show that the wave crest line may reach as long as 250 km (see Figures 1 and 2a). Comparison to theoretical models indicates that the two-dimensional IW structure can well be described by the solitary wave solutions to the Korteweg-de Vries (KdV) equation. The characteristic half widths of the waves are about 0.7 to 1 km [*Zheng et al.*, 2001a].

[3] Of the IW generation mechanism in the NSCS, there are various arguments. *Liu et al.* [1998] and *Hsu and Liu* [2000] suggested that the IWs occurring on the western continental shelf of NSCS (west of Dongsha Island) might be generated by localized boundary conditions. *Ebbesmeyer et al.* [1991] suggested that the long-crested IWs near the Luzon Strait might be generated by tidal current passing through the channels between islands or sills distributed on

[1]Department of Atmospheric and Oceanic Science, University of Maryland at College Park, College Park, Maryland, USA.
[2]Lamont-Doherty Earth Observatory of Columbia University, Palisades, New York, USA.
[3]Department of Marine Environmental Informatics, National Taiwan Ocean University, Keelung, Taiwan.
[4]Jet Propulsion Laboratory, California Institute of Technology, Pasadena, California, USA.

0148-0227/07/2006JC003551$09.00

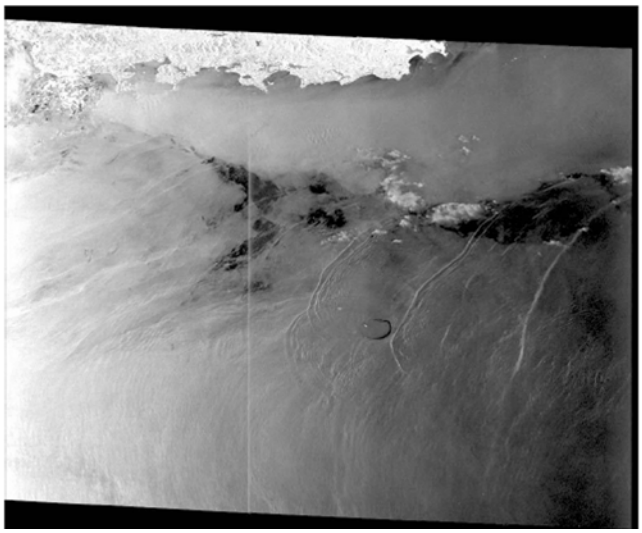

Figure 1. A RADARSAT ScanSAR image of NSCS taken on 26 April 1998 (downloaded from http://www.ifm.uni-hamburg.de). The dark, horseshoe-like feature at the center is imagery of the Dongsha Coral Reef. Grouped bright lines are imagery of IW packets.

the eastern side of the strait. On the basis of the results derived from numerical experiments, *Cai et al.* [2002] suggested the lee-wave generation mechanism for ocean current flowing through three island and sill gaps distributed on the eastern side of Luzon Strait. *Zhao et al.* [2004] suggested a baroclinic tide-topography interaction origin based on the tidal phase analysis of IW satellite imaging time. *Liu et al.* [2004] suggested that strong current from the Kuroshio branching out into the SCS might be a generation mechanism. Recently, *Yuan et al.* [2006] proved that the IWs propagating westward in the Luzon Strait can be induced by the instability of the Kuroshio west wing on the basis of the results derived from the linear wave theories. All the hypotheses have their own bases and reasonableness. However, these hypotheses must face to the same challenge, i.e., how to explain the interannual variability and seasonal variability of IW occurrence frequency, as well as asymmetric distribution of IW packets to the bottom topography? It is the primary motivation for this study to look for other dynamical mechanisms, which are best suitable for description of solitary wave behavior observed in the study area, and give proper explanations to the seasonal variability of solitary wave generation in NSCS.

[4] This paper is organized as follows. The next section gives statistics of spatial and temporal distributions of IW occurrence frequency derived from satellite SAR images. Section 3 analyzes external boundary conditions for IW SAR imaging. In section 4, the physical model and the perturbed KdV equation (PKdV) are adopted to derive the growth condition for solitary IW generation. Section 5 compares theoretical results to the observations. Sections 6 and 7 contain discussion and conclusions, respectively.

2. Statistics of IW Occurrence in NSCS

[5] Previous investigations have demonstrated that the horizontal two-dimensional patterns of ocean IW field and the structure in a wave packet may show up on the SAR images if the sea state is favorable. The IW parameters that can quantitatively be extracted from satellite images include

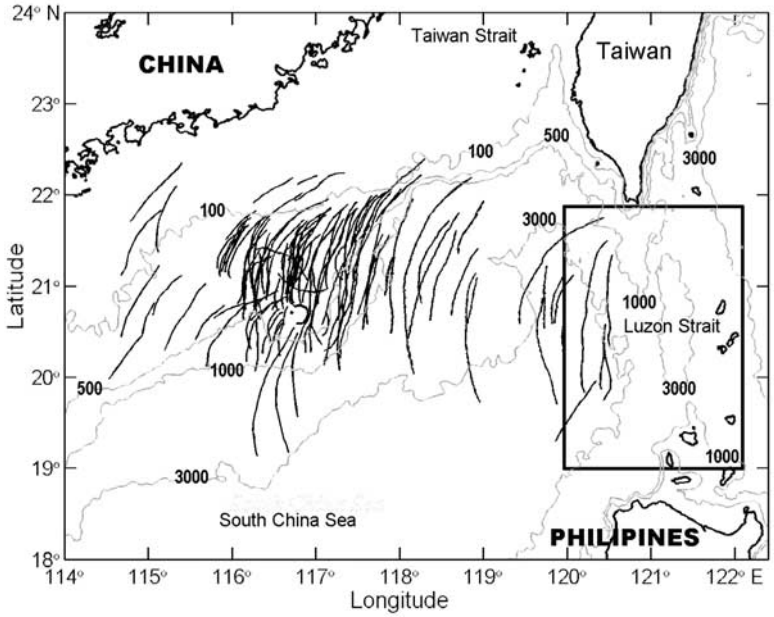

Figure 2a. A map of the study area. Numbers on the isobaths are in meter. Bold lines distributed from 20°N to 22°N represent crest lines of leading waves in IW packets interpreted from SAR images (partially from Figure 1 of *Zhao et al.* [2004]). The rectangular box on the right defines an IW generation source region to be further analyzed in section 4.

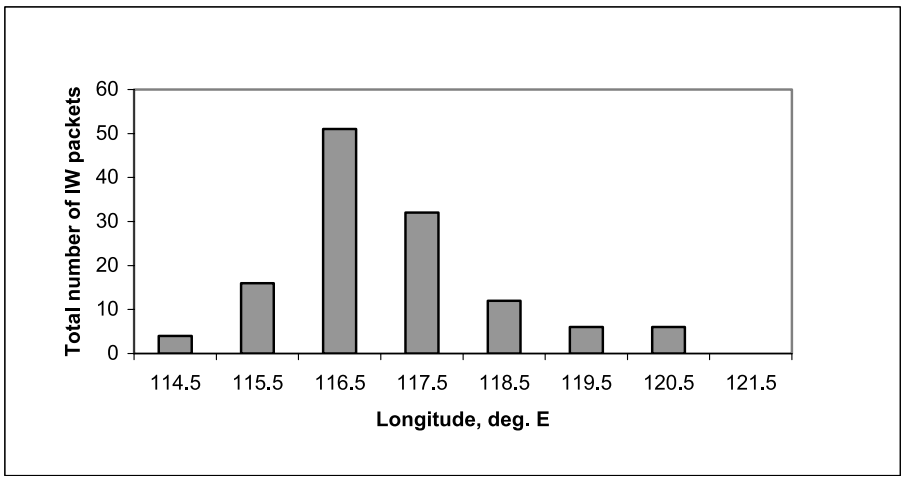

Figure 2b. A histogram of latitudinal distribution of IW packets in NSCS.

the wavelength or separation distance between two consecutive waves, length of crest line, number of solitons in a wave packet, distance between two consecutive wave packets, propagation direction (crest line curvature), polarity (depression or elevation), location, and imaging time [*Zheng et al.*, 1993, 1995]. The characteristic half width of an internal soliton can also be determined from SAR images, then used to calculate the amplitude if ocean stratification parameters are known [*Zheng et al.*, 2001a]. In this section, the SAR images are used for determination of the statistical features of IW occurrence in NSCS.

2.1. Satellite SAR Data

[6] The SAR images taken by ERS-1/2 (European Remote Sensing satellites) serve as a baseline for statistical analysis. The data covering a period of seven years from 1995 to 2001 are collected from public domain including website www.ifm.uni-hamburg.de/ers-sar, National Taiwan Ocean University database, and University of Delaware Internal Wave Data Base. The total 83 images taken on different days with visible IW imagery are collected. In addition, a small number of SAR images taken by RADARSAT (Canadian satellite) and ENVISAT (European Space Agency satellite) are also collected, and related SAR data published by previous investigators [e.g., *Meng*, 2002; *Zhao et al.*, 2004] are cited. Figure 1 shows a sample of satellite SAR images. This is a RADARSAT ScanSAR image taken on 26 April 1998. The imaged area is 528 km by 478 km centered at 21°09′N latitude 116°18′E longitude. The bright area on the top shows the south China coastal region near Hong Kong. The horseshoe-like feature at the center is imagery of the Dongsha Island (small bright spot) and the Dongsha Coral Reef (dark ring). Grouped bright lines distributed in the central portion are imagery of westward propagating IW packets.

2.2. Latitudinal Distribution

[7] A map of our study area with crest lines of leading waves in IW packets, which are obtained from the interpretation of SAR images from 1995 to 2001, is shown in Figure 2a. One can see that almost all IW packets are concentrated within a latitudinal band from 20° to 22°N. All IW packets show the same westward propagation direction. On the east side, the IW packet distribution area is defined by the submarine ridges extending from the southern tip of Taiwan Island all the way crossing the Luzon Strait. A histogram of latitudinal distribution of IW packets with a resolution of 1 degree longitude is shown in Figure 2b. One can see that 22% of IW packets are distributed between 118°E and the west side of the Luzon Strait. No IW is observed on the east side of the strait, implying the Luzon Strait is an origin of these IW packets. The area is a deep basin with little change in the bottom topography. The boundary conditions are favorable for an solitary IW to keep the shape unchanged. Hence the IW packet number and the number of solitons in a packet are much less than that in the shelf break region. While 78% of IW packets are concentrated within a range from 116° to 118°E, which is corresponding to a transit zone from the deep basin to the continental shelf with depths shoaling from 1000 to 100 m. The boundary conditions are favorable for solitary IWs originating from the east boundary to fission and evolve into more packets [*Djordjevic and Redekopp*, 1978; *Zheng et al.*, 2001b].

[8] From the map, one can see that the bottom topography in the source region is generally symmetric about the underwater ridges running north–south. The tidal currents are always reciprocal anywhere, in other words, spatially symmetric to a reference point. Thus the IW packets should be generated symmetrically on both sides of the topography if the tide-topography generation stands as a sole mechanism. However, Figures 2a and 2b show that no any IW packet is found on the east side of the ridges. Obviously, this asymmetric distribution about the bottom topography also constitutes a challenge to the tide-topography generation theories.

2.3. Yearly Distribution of SAR-Observed IW Occurrence Frequency

[9] We have collected seven years of SAR images of IWs in NSCS. It is of interest to see if there is an interannual variability of yearly IW occurrence frequency. For a calen-

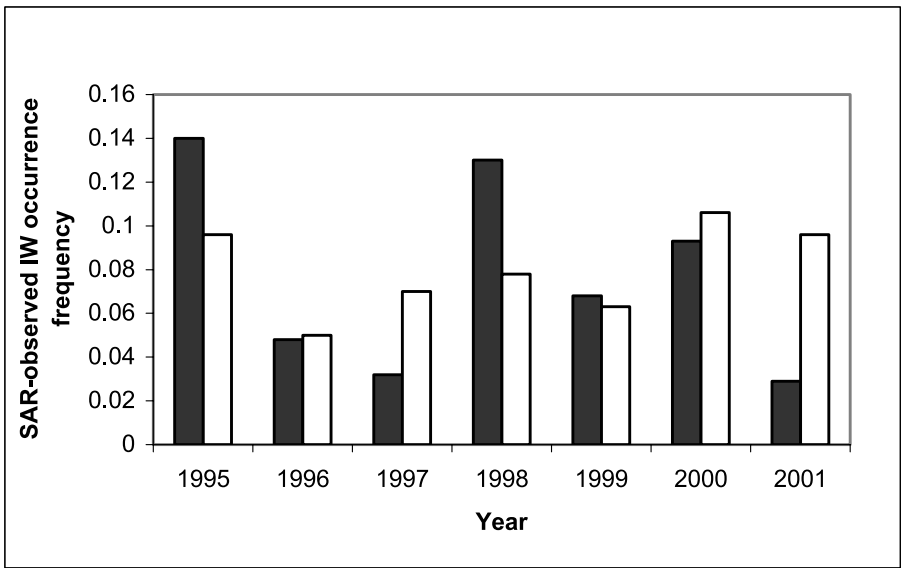

Figure 3a. Yearly distribution of SAR-observed IW occurrence frequencies in NSCS calculated using the full year data collected by this study (dark bars) and by *Meng* [2002] (open bars).

dar year, the SAR-observed IW occurrence frequency is defined as

$$p_i = q_i \left(\frac{N_i}{\sum_j N_j} \right), \tag{1}$$

where N_i (N_j) is a number of days on which the IW is imaged by SAR, here $i(j)$ represents the ith (jth) year, $q_i = D_{1997}/D_i$ as a yearly deweighted factor, here D_{1997} is a number of SAR working days over the study area in 1997, and D_i is the SAR working days in the ith year (71 (1995), 68 (1996), 34 (1997), 57 (1998), 65 (1999), 77 (2000), and 57 (2001), after *Meng* [2002]). The reason to introduce the deweighted factor is that the SAR working days over the study area during the statistical period were not evenly distributed, but varied in different years. The number of SAR working days in 1997 is a minimum, then the yearly deweighted factor for 1997 is taken as 1. The factors for other years are deduced accordingly. The statistical results are shown in Figure 3a. One can see an obvious interannual variability of SAR-observed IW occurrence frequency in NSCS. In 1995, 1998, and 2000, the frequencies are 2 to 4 times higher than that in other years.

[10] On the other hand, the SAR working days used in the statistical calculation are inhomogeneously distributed in a year; and the SAR-observed IW occurrence frequencies have the seasonal variability as discussed in the next section. These two points might cause the statistical error to the interannual variability. In order to further confirm the existence of the interannual variability, the IW occurrence frequency (IW occurrence days divided by SAR working days) in an occurrence peak phase from April to July each year is calculated. The results are shown in Figure 3b. One can see that the interannual variability is still there. In 1995, 1998, and 2000, the frequencies are obviously higher than other years. This interannual variability implies that there are long-term and large-scale processes playing roles in

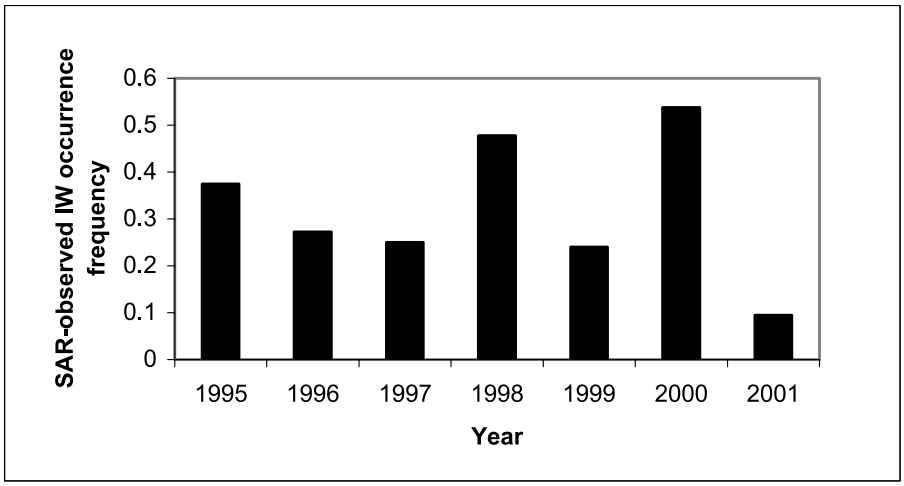

Figure 3b. Same as Figure 3a, but using the data from April to July only.

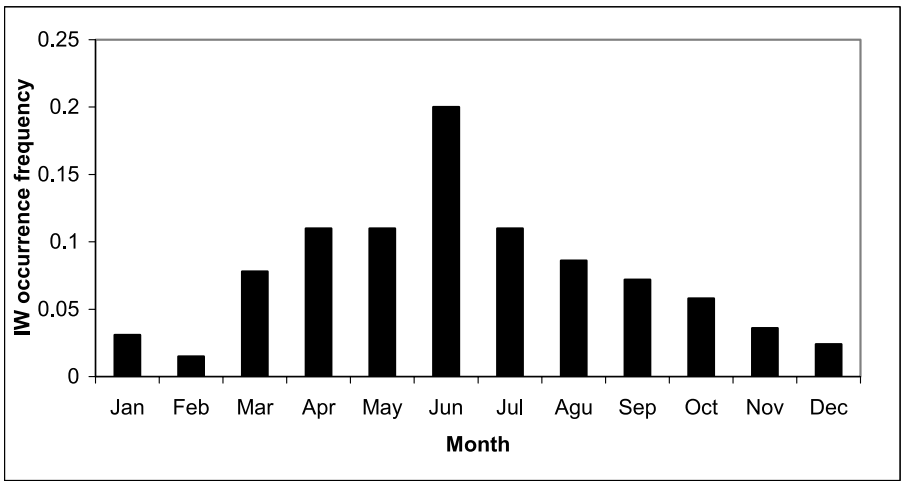

Figure 4a. Monthly distribution of SAR-observed IW occurrence frequencies in NSCS.

modifying IW occurrence frequency and SAR imaging in NSCS.

2.4. Monthly SAR-Observed IW Occurrence Frequency

[11] The monthly SAR-observed IW occurrence frequency is defined as

$$p_{mi} = q_{mi}\left(\frac{n_i}{\sum_{j=1}^{12} n_j}\right), \tag{2}$$

where n_i (n_j) is a number of total days in the ith (jth) month of 7 years, at which the IWs were imaged, and $q_{mi} = d_8/d_i$ as a monthly deweighted factor, here d_8 is a minimum number of SAR working days over the study area in August, and d_i is the SAR working days in the ith month. The calculation results are shown in Figure 4a. Considering the dependence of SAR imaging on the sea states (see the next section for details), the calculation results are further deweighted by the low sea state frequencies (for wave height less than 1.9 m). The method is to multiply a deweighted factor of f_m/f_i, in which f_m is the maximum frequency of low sea states, and f_i is the frequency in ith month. The results are shown in Figure 4b. One can see that both statistical results give similar and obvious seasonal variability. The high occurrence frequencies are distributed from April to July and reach a peak in June with a maximum frequency of 20%. The low occurrence frequencies are distributed in winter from December to February of next year with a minimum frequency of 1.5% in February. Other months appear to be transit periods. In the next two sections, the external and internal causes leading to this uneven distribution will be examined.

3. Statistical Analysis of External Boundary Conditions for IW SAR Imaging

[12] As mentioned above, the IW occurrence frequencies shown in Figures 4a and 4b are derived from SAR images. According to SAR imaging theories, however, only low wind and low sea state conditions are favorable for IW imaging [*Zheng et al.*, 2001a]. The statistical distributions of these two conditions may serve as dynamical filters to modify the SAR-observed IW occurrence frequency. How-

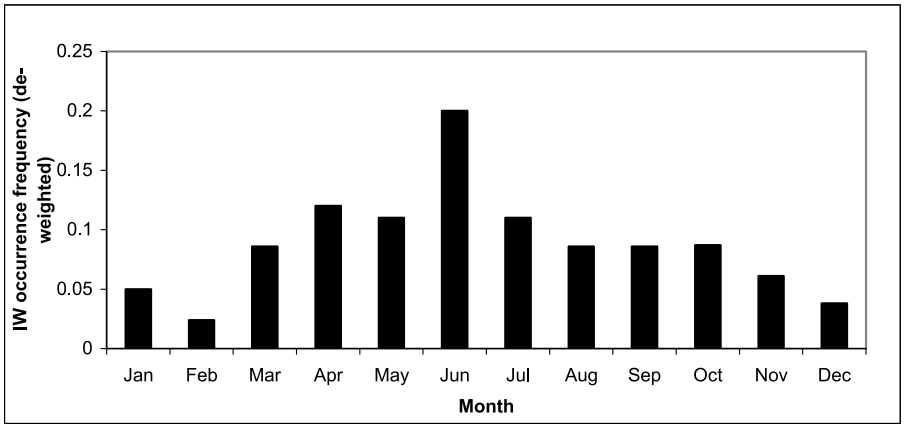

Figure 4b. Same as Figure 4a, but deweighted by low sea states.

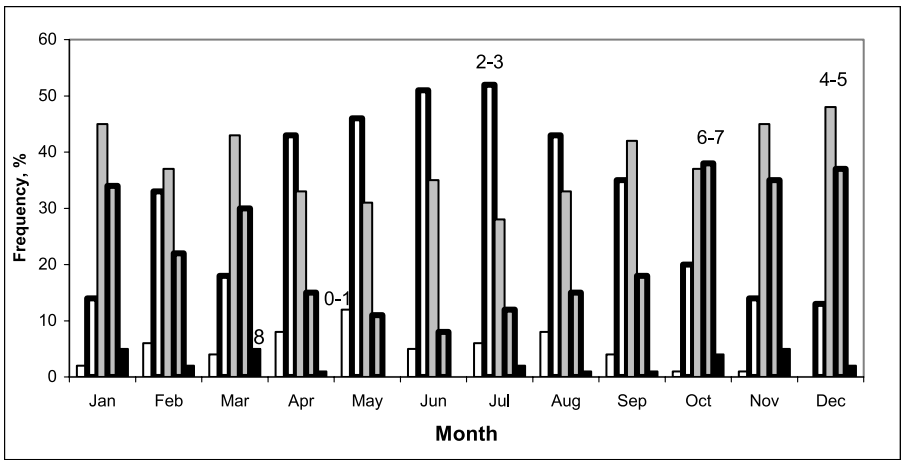

Figure 5. Statistical distributions of monthly mean wind frequencies at statistical cell centered at 22°N 118°E in NSCS. The numerals marked at peak bars represent wind scale ranges. Statistical errors are less than 1%.

ever, the two conditions do not constitute immediate forcing to generate the waves.

3.1. Wind Condition Statistics

[13] Winds over the study area are dominated by the East Asia monsoon. In summer (JJA) the southwesterly winds with an average wind speed of 6 m s^{-1} dominate. In winter (DJF) the wind direction totally reverses, northeasterly winds with an average speed of 9 m s^{-1} prevail over the whole region [*Pohlmann*, 1987; *Shaw and Chao*, 1994; *Metzger and Hurlburt*, 1996]. Statistical distributions of monthly mean wind frequencies are derived from long-term historical data sets of field observations [*Editorial Group of Marine Climate Atlas of Institute of Geography*, 1982]. Statistical cells of 2° latitude by 2° longitude were used in the data sets. The cell centered at 22°N 118°E is chosen to represent the study area. The results are shown in Figure 5. One can see the seasonal variability of wind scales. High frequencies of low wind conditions (scales 0–1 and 2–3, equivalent to the wind speed lower than 5 m s^{-1}) are distributed from April to September and reach a peak phase from May to July with a maximum frequency of 58% in July. The low frequencies are distributed from November to March of next year. The frequency distributions of high wind conditions (scales 4–5, 6–7, and 8, equivalent to the wind speed higher than 5 m s^{-1}) are just antiphase with low wind conditions. High frequencies are distributed from October to next March and reach a peak phase from November to next January with a maximum frequency of 87% in December.

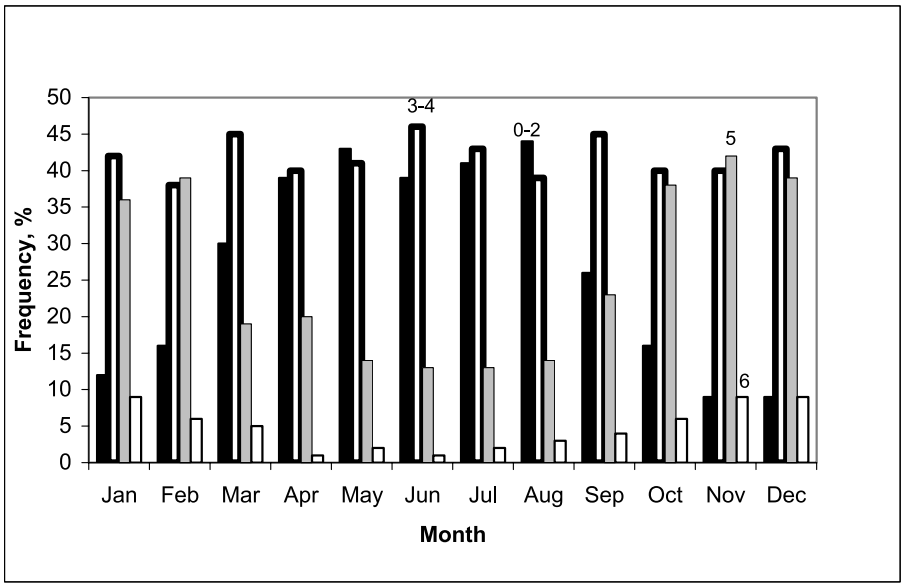

Figure 6. Statistical distributions of monthly mean sea state frequencies at the statistical cell centered at 22°N 118°E. The numerals marked at peak bars represent wave scale ranges. Statistical errors are less than 1%.

Table 1. Correlation Coefficient and Confidence Level of the SAR-Observed IW Occurrence Frequency With the Monthly Mean Sea Surface Wind and the Monthly Mean Sea State

	Wind Scale				
	0–2	3–4	4–5	6–7	8
Wind speed, m s^{-1}	0–1	2–5	6–10	11–17	≥18
Correlation coefficient	0.489	0.766	−0.610	−0.766	−0.598
Confidence level	>80%	>99%	>95%	>99%	>95%
	Wave Scale				
	0–2	3–4	5	6	
Wave height, m	0–0.7	0.8–1.9	2.0–3.4	3.5–6.0	
Correlation coefficient	0.792	0.478	−0.823	−0.844	
Confidence level	>99%	>80%	>99%	>99%	

3.2. Sea State Statistics

[14] Statistical distributions of monthly mean sea state frequencies are derived from the long-term historical data sets of field observations in the same literature as the wind data and at the same statistical cell. The statistical distribution of monthly sea state frequencies is shown in Figure 6. One can see that high frequencies of wind wave scales 0–2 (for the wave height less than 0.7 m) are distributed from April to August and reach a peak value of 44% in August. The low frequencies are distributed from October to next February with frequencies lower than 16%. March and September appear as transit phases. The frequencies of scales 3–4 (for the wave height from 0.8 to 1.9 m) have an almost even distribution with a mean of 41.8% and a standard deviation of 2.5%. The distributions of scales 5 (for the wave height from 2.0 to 3.4 m) and 6 (for the wave height from 3.5 to 6.0 m) are antiphase with scales 0–2.

[15] In order to estimate the dependence of IW SAR imaging on the sea surface boundary conditions, we calculate the correlation coefficient and confidence level of the SAR-observed IW occurrence frequency shown in Figure 4a with the sea surface wind scale shown in Figure 5 and the sea state scale shown in Figure 6. The results are listed in Table 1. One can see that for the wind scale, the highest correlation coefficient (0.766) and the highest confidence level (>99%) occur at wind scale 2–3, not at the lowest wind scale 0–1. The reason may be that at the lowest wind scale, there are no enough small waves generated on the sea surface, which serve as major backscatterers of radar pulses. For the sea state, the highest correlation coefficient (0.792) and the highest confidence level (>99%) occur at the lowest sea state scale. The negative correlation coefficients mean that the two processes vary out of phase (phase difference of π); that is, the higher wind speed and sea state frequencies, the lower SAR-observed IW occurrence frequencies.

4. Dynamical Analysis of IW Generation

[16] The statistical results in section 3 indicate that there are two possibilities. (1) The seasonal fluctuation of wind and sea state conditions in NSCS may be factors to modify monthly distribution of SAR-observed IW occurrence frequency. (2) The two processes coincide with IW occurrence, and play roles like time-dependent band-pass filters in IW imaging time series. As external factors, however, the sea states only decide the observable conditions, do not immediately generate the ocean internal waves. Thus internal decisive factors for IW generation should be located. To date, all IW theories, no matter linear or nonlinear, have verified that the ocean vertical stratification is a decisive factor for IW propagation [*Phillips*, 1977; *Ostrovsky and Stepanyants*, 1989]. In this section, one can see that a horizontally varying stratification, i.e., an inhomogeneous thermocline, plays a decisive role in solitary IW generation.

[17] On the basis of the above observations and statistical analyses, the following hypotheses are proposed. The solitary internal waves are generated in a certain area defined as a source region. The source region, working like an oscillator, has the potential to provide the necessary and sufficient conditions for wave generation: (1) initial disturbance formation and (2) wave amplitude growth. The source region also dissipates the disturbance energy, so that only fully developed waves are able to radiate out of the source region.

[18] In this study, the tides, tide-topography interaction, west boundary current instability, and others are treated as the necessary conditions for initial disturbance formation, but they are not the sufficient conditions for IW generation. The sufficient conditions will be examined later on.

4.1. Physical Model and Scale Analysis

[19] According to the collected SAR observations shown in Figures 2a and 2b, we propose the Luzon Strait area enclosed by latitudinal lines of 20°N and 21°50′N, and longitudinal lines of 120° E and 122°E, as marked by a

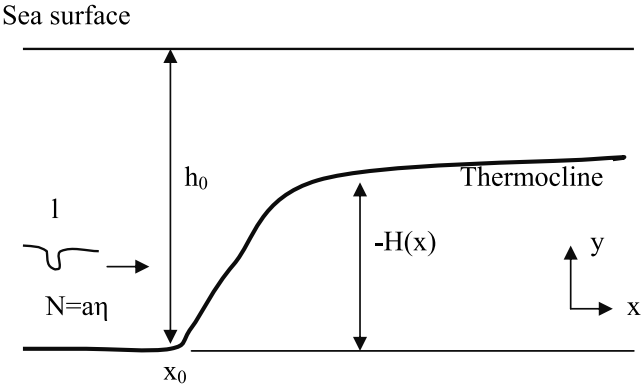

Figure 7. A schematic of physical model for internal solitary wave generation in the source region shown in Figures 2a and 2b. The x axis is westward positive, and the y axis is upward positive.

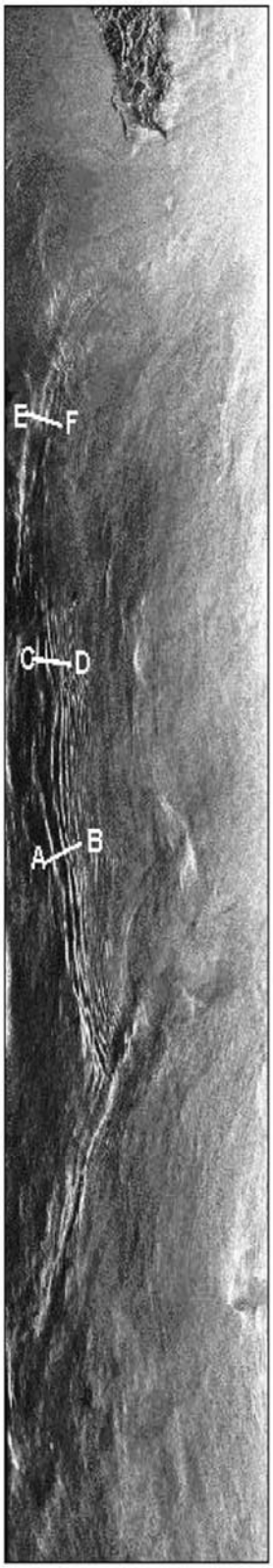

Figure 8a. A composite of four standard scenes of ERS-1 SAR images in the source region of this study taken at 02:29 UT on 16 June 1995. The dark area on the top is the imagery of the southern tip of Taiwan Island. Grouped bright lines are imagery of solitary IW packets propagating westward.

rectangular box on the right of Figure 2a, to be an IW generation source region. A physical model used to describe the problem of IW generation is shown in Figure 7. The x axis is westward positive, and the y axis is upward positive. The model ocean is vertically stratified into two layers by a thermocline. The deeper layer has an infinite depth. The depth of upper layer is a constant h_0 for $x < x_0$, and variable as $h_0 - H(x)$ for $x \geq x_0$. An initial solitary disturbance with an amplitude N and a width l is formed at $x = x_0$ and propagating along the thermocline. The characteristic scales are analyzed as follows. The depth of 15°C isotherm is defined as the depth of thermocline. The scale of upper layer depth derived from the observed stratification data (see Figure 9 later in this section and Figures 11a–11d in section 5.1) is determined as $h_0 = \mathrm{O}(200\ \mathrm{m})$. From SAR images as shown in Figure 8a, the characteristic half width of the leading soliton is around 2 km [*Zheng et al.*, 2001a; *Yuan et al.*, 2006], thus the length scale of soliton is determined as $l = \mathrm{O}(2\ \mathrm{km})$. The average depth of source region is 2000 m. Using these data, therefore, the amplitude scale of soliton can be estimated as $a = \mathrm{O}(30\ \mathrm{m})$ [*Zheng et al.*, 2001a]. Thus these characteristic scales satisfy the scale balance relations $h_0^2/l^2 = \varepsilon = 0.01 \ll 1$, and $a/h_0 = \mu = 0.15 \ll 1$.

[20] Physically, the internal soliton growth problem of interest is equivalent to the evolution problem of surface soliton propagating along a shoaling beach [*Zheng et al.*, 1998]. In this case, the soliton amplitude satisfies the perturbed KdV equation [*Newell*, 1985],

$$q_\tau + 6qq_\theta + q_{\theta\theta\theta} = -\frac{9}{4}\frac{D_\tau}{D}q, \tag{3}$$

where τ is a rescaled distance coordinate,

$$\tau = \frac{1}{6}\int^X D^{1/2}dX, \tag{4}$$

θ is the retarded time,

$$\theta = -t + \frac{1}{\varepsilon}\int^X \frac{dX}{D^{1/2}}, \tag{5}$$

where t is the time, D is the nondimensional depth of the upper layer, $D = 1 + h$, in which $h = H(x)/h_0$, $X = \varepsilon x$, and the subscript represents partial differential with respect to that variable.

[21] Solutions of (3) can be expressed as

$$q(\theta,\tau) = q^{(0)} + \sigma q^{(1)} + \ldots, \tag{6}$$

where

$$q^{(0)} = 2\eta^2\mathrm{sech}^2\eta\left(\theta - 4\eta^2\tau - \theta_0\right), \tag{7}$$

in which η is the amplitude parameter, a slowly varying function of the distance, and θ_0 is the initial retarded time, and

$$q^{(1)} = \frac{\Gamma}{6\eta}\{-1 + \tanh\eta\xi + \mathrm{sech}^2\eta\xi(3 - 3\eta\xi\tanh\eta\xi + 2\eta\xi - 2\eta^2\xi^2\tanh\eta\xi)\} + \frac{\Gamma}{2}(1 - \tanh\eta\xi)\mathrm{sech}^2\eta\xi, \tag{8}$$

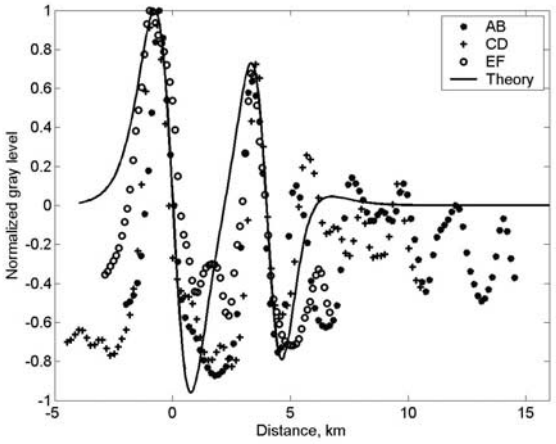

Figure 8b. A comparison of the PKdV solitary wave solutions (curve) to the SAR-observed ocean internal wave packets (data points) in the Luzon Strait. The imagery gray level data are taken from three transects, AB, CD, and EF, as marked on the image in Figure 8a.

where

$$\Gamma = \frac{9}{4}\frac{D_\tau}{D}, \tag{9}$$

and $\xi = \theta - \overline{\theta}$ is a time variable in a coordinate system moving with the solitary wave, and σ is the order of Γ [= O(0.3) in the studied case] satisfying $0 < \varepsilon \ll \sigma \ll 1$. Solutions (7) and (8) represent a large soliton with a small oscillatory tail (Figure 8b). As seen later, the initial solitary disturbance will grow and gradually evolve into a solitary wave packet as propagating along the shoaling thermocline.

[22] Figures 8a and 8b shows an example of solitary wave packet, which has fully grown and radiated out of the source area. The case was imaged by ERS-1 SAR over the Luzon Strait at 02:29 UT on 16 June 1995. The SAR swath of about 100 km by 400 km scans the strait from the north to the south. The dark area on the top is the imagery of the southern tip of Taiwan Island. One can see that on the west (left) side of the image there is an internal wave packet led by a soliton with a crest line as long as 200 km, and followed by a group of small waves with an average wavelength of about 1 km and gradually shortened crest lines. The westward curvatures of the crest lines imply that the packet propagates westward. In order to compare the structure of this packet with theoretical solutions (7) and (8), the solutions are transformed to the forms of the SAR image [*Zheng et al.*, 2001a]. The parameters are chosen as follows: $\Gamma = 0.3$, $\sigma = 0.3$, $\eta = 0.42$, t = 0, $\theta_0 = 0$, $\overline{\theta} = 8$, and the distance scale is 0.5 km. A normalized waveform is shown in Figure 8b as a curve. The data points are gray level values taken from the transects marked on Figure 8a, corrected by SAR incidence angle, and normalized by the maximum values. Here the SAR system is assumed as a linear sensor, then the gray level values of SAR imagery are used to represent the radar return intensity [*Zheng et al.*, 2001a]. One can see that the theoretical solutions describe the major features of observed solitary wave packet well. The location of the leading soliton with respect to the shoaling thermocline is shown in Figure 9. One can see that the leading soliton has climbed up to the shallow side of the upper layer.

4.2. Parameterization for Soliton Amplitude Growth

[23] It is very important to note the solvability of equation (3), which demands [*Newell*, 1985]

$$\frac{\partial \eta}{\partial \tau} = -\frac{2}{3}\Gamma\eta. \tag{10}$$

Transforming (10) into the *x*-*y* coordinates yields

$$\frac{d\eta}{dx} = \left(-\frac{3}{2D(x)}\frac{dD(x)}{dx}\right)\eta. \tag{11}$$

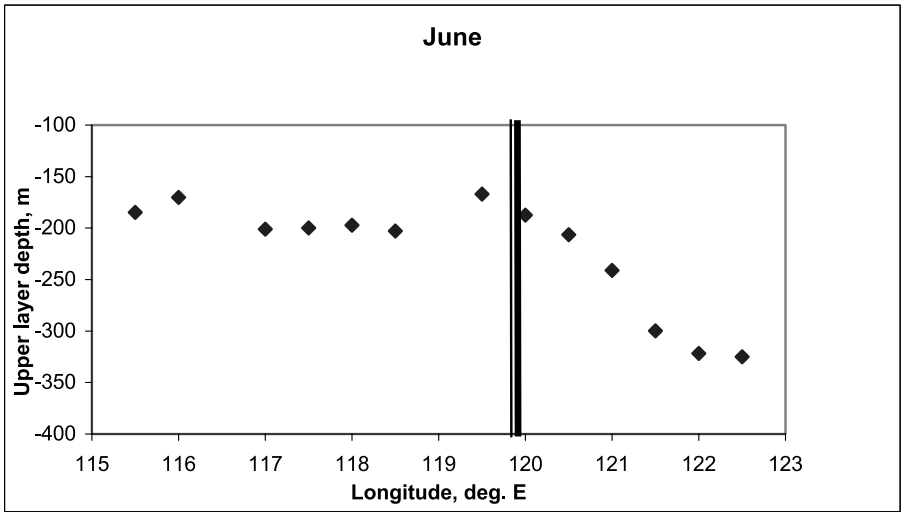

Figure 9. Monthly mean upper layer depth of June in NSCS (see section 5.1 for details). The statistical errors are less than 2 m estimated by the depth accuracy of temperature profilers. Double vertical lines near 120°E represent the location of leading soliton shown in Figure 8a.

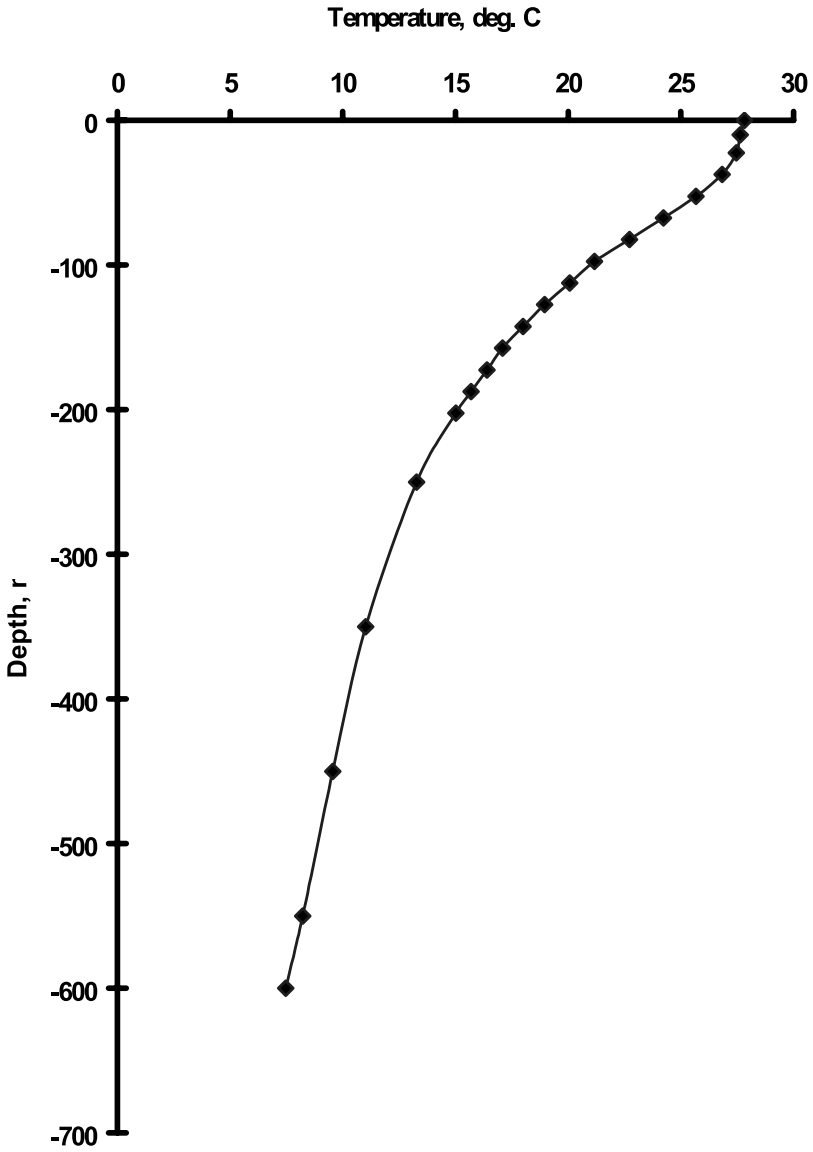

Figure 10. A 20-year mean temperature profile in the SCS.

The solution of (11) is

$$\eta = \eta_0 D(x)^{-3/2}, \tag{12}$$

where η_0 is the initial solitary disturbance amplitude at x_0. On the basis of (12), we parameterize a soliton amplitude growth ratio (SAGR) as $\beta(x) = \eta/\eta_0$, then we have

$$\beta(x) = D(x)^{-3/2}. \tag{13}$$

[24] To simplify the analysis, equation (3) does not include a dissipation term. In a real ocean, however, the dissipation induced by the eddy viscosity and bottom friction [*Liu et al.*, 2004], and wave-induced mixing in the upper ocean [*Qiao et al.*, 2004] always exist. In our case, particularly, the length of soliton growth zone or thermocline shoaling area is as long as 200 km as shown in Figures 2a, 2b, and 9, the dissipation effect cannot be ignored. Therefore the SAGR becomes a necessary condition to overcome the dissipation effect. In other words, not all the initial disturbances may grow up and be finally radiated out of the source region, depending on the balance between the growth and dissipation. This may be verified by the low monthly SAR-observed IW occurrence frequency shown in Figure 4a and 4b. The maximum monthly occurrence frequency in a year is only 20% in June, although the tidal disturbance occurs daily and the favorable sea state frequency is as high as 40%. Thus the IW occurrence frequency p in NSCS (beyond the source region) should be proportional to the SAGR at the source region boundary, i.e.,

$$p = a\beta(x_{up}) - b, \tag{14}$$

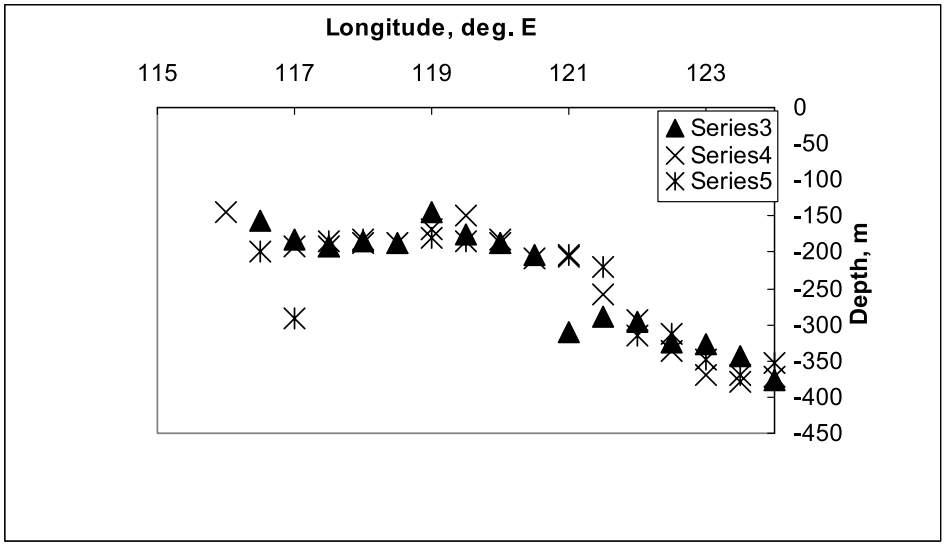

Figure 11a. Monthly mean upper layer depths in NSCS in spring (MAM) derived from water temperature profiles measured from 1980 to 1993 archived in NOAA NODC. The statistical errors are less than 2 m.

where x_{up} represents the location of source region boundary, a and b are constants. Nonzero constant b implies that the IW occurrence needs a threshold value of SAGR.

5. Comparison to Field Measurements

[25] Equation (14) indicates that the IW occurrence frequency can be predicted if the SAGR is known. On the other hand, monthly SAR-observed IW occurrence frequencies in NSCS have been derived from statistics of SAR images in section 3. The SAGR can be derived from thermocline depth measurements within the source region. Thus equation (14) can be validated.

5.1. Ocean Stratification Data

[26] The ocean water temperature profile data are provided by NOAA (National Oceanic and Atmospheric Administration) NODC (National Oceanographic Data Center). The data were measured by conductivity-temperature-depth (CTD) profilers, the mechanical (MBT), expendable bathythermographs (XBT), and digital bathythermographs (DBT) [*Boyer and Levitus*, 1994]. After data processing, a total of 17,528 hydrographic profiles from January 1980 through December 1999 are obtained. Figure 10 shows a typical example of the profiles, which is a 20-year mean temperature profile in the SCS.

[27] From Figure 10, one can see that the temperature profile, in fact, is continuously stratified. A top layer of about 40 m is basically homogeneous with an average temperature of 27.3°C. Below the top layer, there is a thermoline with a steep temperature decrease of 14.0°C, say at 250 m. To simplify the dynamical analysis, this continuously stratified ocean is sometimes treated as a two layer ocean. To determine the upper layer thickness,

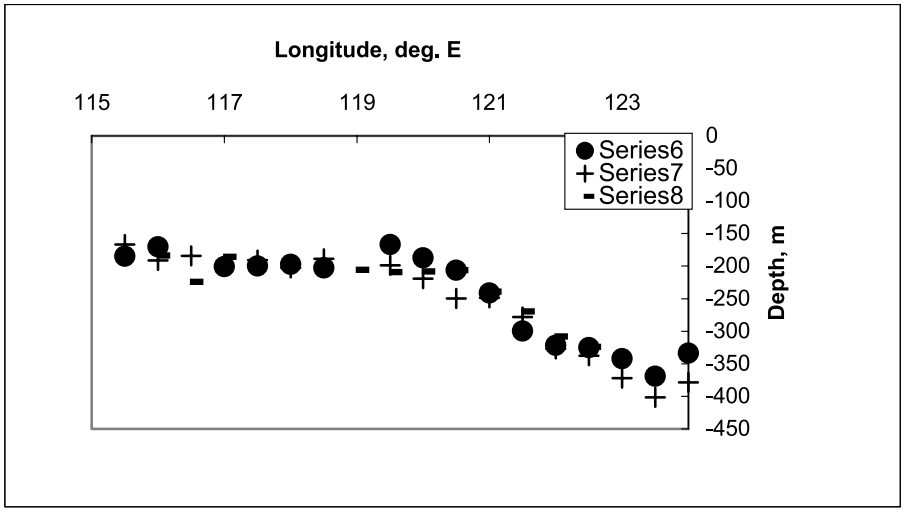

Figure 11b. Same as Figure 11a, but in summer (JJA).

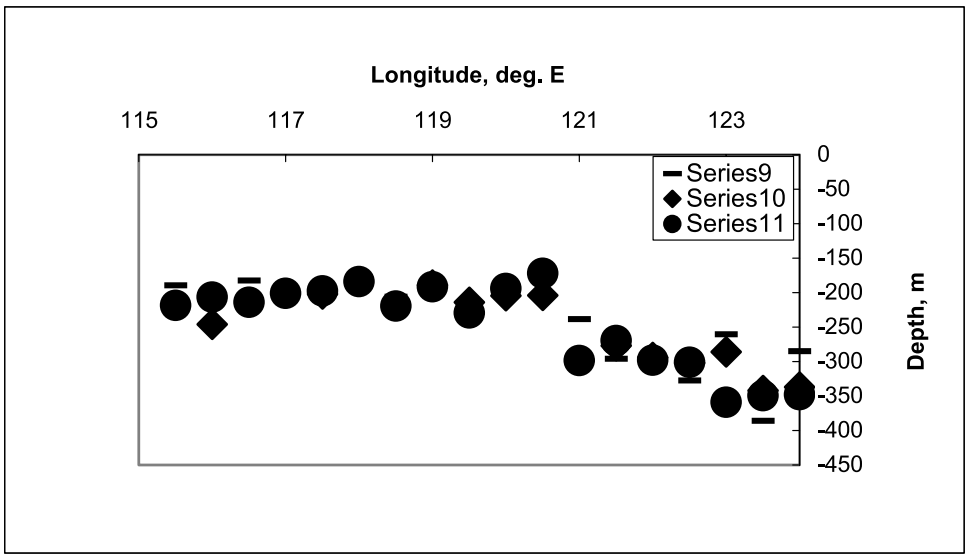

Figure 11c. Same as Figure 11a, but in fall (SON).

previous investigators chose different standards. For the tropic oceans, *Worthington* [1959] and *Wang et al.* [2000] used the depths of 18°C and 20°C isotherms as the thermocline depths, respectively. *Meyers* [1979] and *Wang and McPhaden* [2000] used the depth of 14°C isotherm as the thermocline depth. Our study area, NSCS, is located in the subtropic region. In order to determine an isotherm to represent the upper layer depth in NSCS, we did sensitivity tests using 14°C, 15°C, and 16°C isotherms, because the three temperatures are located near the turning point of temperature profile. The correlation analysis of SAGR derived from the upper layer depths determined by the three isotherms to the IW occurrence frequency gives similar results. Thus, taking the mean, the depth of 15°C isotherm is defined as the thermocline depth. Thus the thickness from the sea surface to the depth of 15°C isotherm is defined as the upper layer depth. The data within a band of (21° ± 1°)N from 116°E to 122.5°E are used to generate monthly mean upper layer depths with a resolution of 2° latitude by 0.5° longitude, which are used to represent ocean stratification in NSCS. The results are shown in Figures 11a–11d. Comparing with the physical model shown in Figure 7, the x axis should be arranged from east to west and in a reverse order of longitudes.

5.2. Soliton Amplitude Growth Ratio

[28] Using the data taken from Figures 11a–11d and comparing to the physical model shown in Figure 7, the SAGR is calculated by

$$SAGR = \left(\frac{h_0}{d}\right)^{3/2}, \tag{15}$$

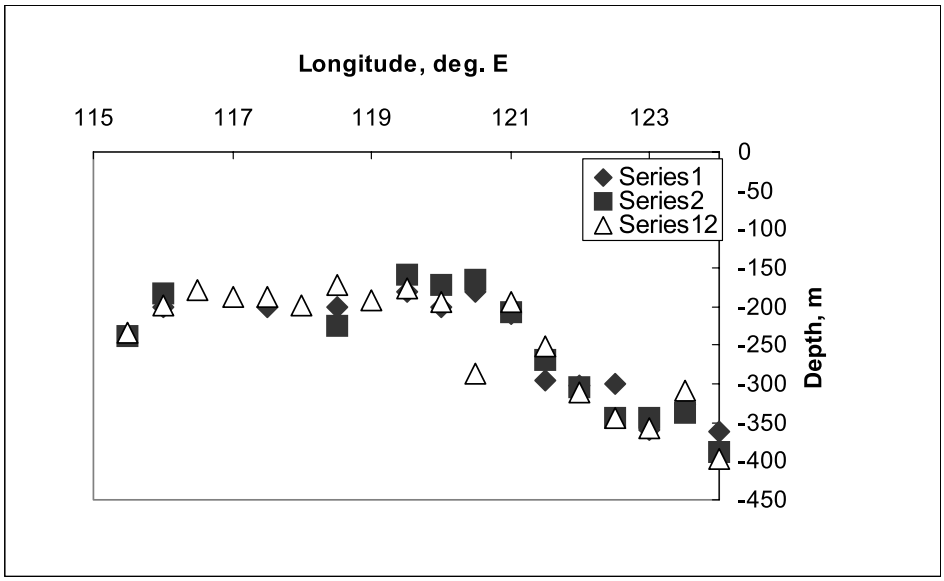

Figure 11d. Same as Figure 11a, but in winter (DJF).

Table 2. Monthly Mean SAGR in the Source Region Calculated From the Shoaling Thermocline Defined by 15°C Isotherm

	h_0		d		SAGR	
Month	Location, °E	Depth, m	Location, °E	Depth, m	Mean	SDV
Jan	122	302	120.5	180	2.17	0.22
Feb	122.5	344	120.5	165	3.01	0.30
March	121	310	119.5	185	2.17	0.22
April	122.5	336	119	169	2.80	0.28
May	123	349	119	180	2.70	0.26
June	123	342	119.5	167	2.93	0.29
July	123	372	119.5	199	2.56	0.26
Aug	122.5	324	120.5	207	1.96	0.20
Sep	122	327	120.5	207	1.99	0.20
Oct	122.5	302	120.5	204	1.80	0.18
Nov	122.5	301	120	194	1.93	0.19
Dec	122	311	119.5	175	2.37	0.24

where h_0 and d are the upper layer depths on the deep side and shallow side of the shoaling thermocline defined by 15°C isotherm, respectively. The measurements and calculation results are listed in Table 2 and illustrated in Figure 12, in which the results derived from thermocline defined by 14°C and 16°C isotherms are shown for comparison.

[29] The correlation coefficient and confidence level between the monthly SAR-observed IW occurrence frequency and SAGR reveal two important facts. (1) The two full year data sets only generate a correlation coefficient of 0.403, while the correlation coefficient increases to 0.845 with a confidence level of >99%, if excluding the winter months (DJF). The probable reason is that IW occurrence frequency is underestimated by SAR observations owing to high occurrence frequencies of unfavorable high sea states in winter. (2) The upper layer depths defined by 14°C and 16°C isotherms give similar results to that defined by 15°C.

[30] The monthly SAR-observed IW occurrence frequency (shown in Figure 4b) versus the monthly mean SAGR (except winter months) derived from upper layer depths defined by 14°C, 15°C, and 16°C isotherms is plotted in Figure 13. One can see that as a first-order approximation, the theoretical model (linear relation) gives a trend of data points with a correlation coefficient (R^2) of 0.6519 (15°C data). The regression equation is

$$P_s = 0.0744 SAGR(\beta) - 0.0677, \tag{16}$$

which has the form as predicted by (14). From (16), the threshold value of SAGR(β), which is defined as an SAGR value for the IW occurrence frequency equal to zero, is 0.90.

6. Discussion

6.1. Of Interannual Variability of SAR-Observed IW Occurrence Frequency

[31] The interannual variability of SAR-observed IW occurrence frequency in NSCS is an important discovery of this study, although the two data sets in Figure 3a and 3b show a little difference due to limited samples. This study also finds the sea states are major external conditions to modify the SAR-observed IW occurrence frequency, and thermocline shoaling provides internal forcing to IW generation. Therefore they should have links with the interan-

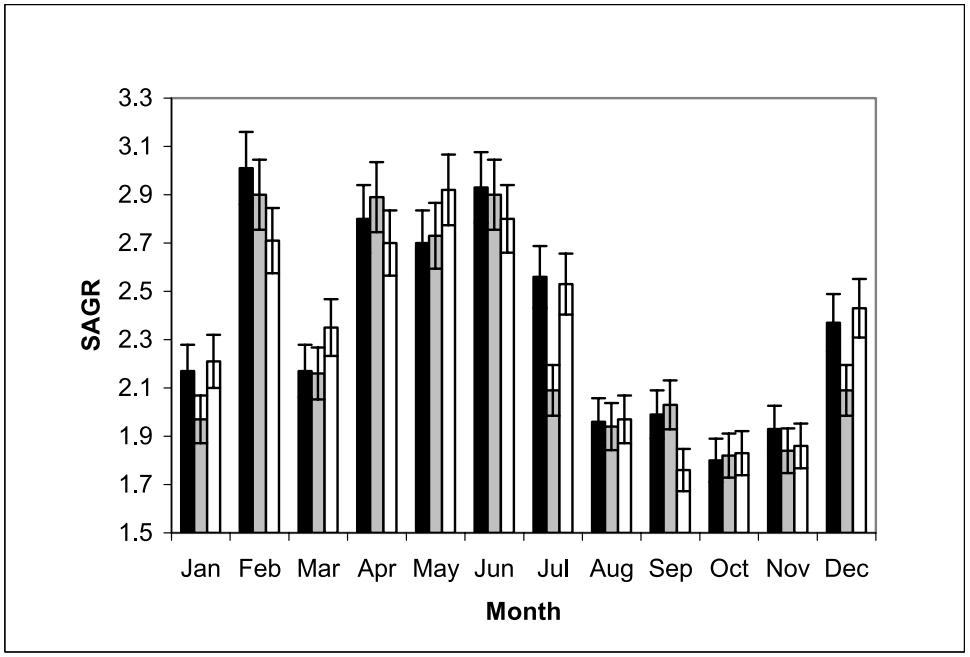

Figure 12. Monthly mean SAGR in the Luzon Strait, the source region of this study, derived from the temperature profile data from 1980 to 1993. Dark bars are derived from the upper layer depth defined by 15°C isotherm, and gray and open bars are from 14°C and 16°C isotherms, respectively. The error bars show a maximum error of 10%.

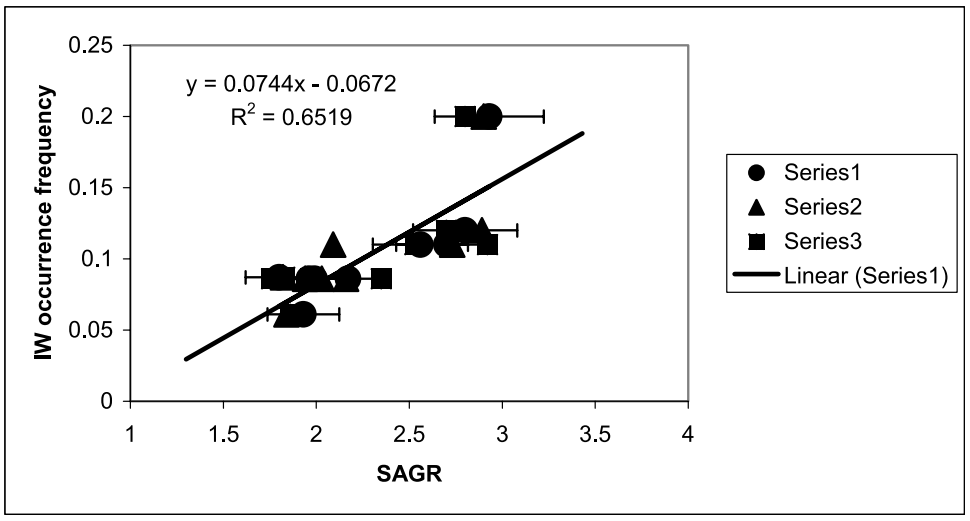

Figure 13. The monthly IW occurrence frequency versus the monthly mean SAGR in NSCS (no winter months DJF included). The straight line is derived from a linear regression of the data listed in Table 2 (series 1, 15°C thermocline). The data points derived from 14°C (series 2) and 16°C (series 3) are also plotted for comparison. The error bars represent an estimated maximum error of 10%.

nual variability of IW occurrence frequency. In the future studies, we will pursue further evidence to clarify the links.

[32] The Kuroshio, a strong western boundary current flowing northward along the east side of the Luzon Strait, is another key element, which may play a significant role in modifying the SAR-observed IW occurrence frequency in NSCS. Previous investigations have found that both Kuroshio axis and front oscillate seasonally into and out of the Luzon Strait. Even there is a Kuroshio branching intruding into the NSCS through the Luzon Strait especially in winter [*Guo et al.*, 2004]. The intrusion is enhanced during the La Nina periods [*Ho et al.*, 2004]. These dynamical processes certainly have direct contribution to the variation of vertical and horizontal stratification structure, including the steepness of thermocline, which is a decisive forcing for solitary IW growth as analyzed in this study. According to *Yuan et al.* [2006], the Kuroshio is also an initial IW disturbance source caused by its current instability, and may play a role in eliminating the growth possibility for the eastward propagating initial disturbances. These interesting topics are worthy to be further studied if complete field observation data sets are available.

6.2. Of Eastward Propagating Initial Disturbance

[33] As mentioned in section 2.2, the bottom topography in Luzon Strait as shown in Figure 2a is near symmetric about the north–south submarine ridges, and the tidal flows are reciprocal anywhere. Thus tide-topography interaction should have the same probability to induce the westward and eastward propagating initial disturbances. The analysis in section 4 indicates that the westward propagating initial disturbances indeed obtain a chance to grow up and to radiate out of the source region. However, the eastward propagating initial disturbances run into a deepening thermocline. According to (13), the deepening thermocline cannot provide the boundary conditions for the solitary wave growth. So that the eastward propagating initial disturbances may not overcome the dissipation effect, and may not radiate out of the source region. This explains the asymmetric latitudinal distribution of IW packets in NSCS shown in Figures 2a and 2b.

6.3. Parallel Method for Deriving SAGR

[34] The SAGR can also be derived from the Schrödinger eigenvalue problem [*Tappert and Zabusky*, 1971; *Zheng et al.*, 2001b]. For the first soliton, we obtain SAGR (a_1) in the form of

$$a_1 = \left[\frac{\left(1+8\beta^2\right)^{1/2}-1}{2\beta}\right]^2, \tag{17}$$

where β is the same as defined by (13) of this paper. Using the data in Table 2, monthly mean SAGR (a_1) is calculated. The results are listed in Table 3. One can see that monthly mean SAGR (a_1) has the same seasonal variability trend as SAGR (β) listed in Table 2, but the mean (1.47 ± 0.07) is 38% smaller than that of SAGR (β) (2.37 ± 0.40).

6.4. Comparison to Other Statistical Results

[35] *Meng* [2002] and *Zhao* [2004] also independently did statistics of monthly SAR-observed IW occurrence frequencies in NSCS. Their monthly SAR-observed IW occurrence frequency versus the monthly mean SAGR from March to November derived from this study also give good linear relations as predicted by theoretical model (14). The threshold values of SAGR (b/a) are 0.59 and 1.36, respectively, further evidencing the SAGR threshold as an important dynamical condition for IW generation in the Luzon Strait.

7. Conclusions

[36] In this study, satellite SAR images and field measurements, statistical analysis and dynamical analysis are com-

Table 3. Monthly Mean SAGR (a_1) Calculated by Equation (17)

Month	a_1
Jan	1.45
Feb	1.58
March	1.45
April	1.55
May	1.43
June	1.57
July	1.52
Aug	1.40
Sep	1.40
Oct	1.35
Nov	1.39
Dec	1.49

bined to find convincible explanations to the ocean internal wave generation mechanisms in the north South China Sea. The major results of this effort are summarized as follows.

[37] Latitudinal distribution statistics indicate that 22% of IW packets are distributed between 118°E and the west side of the Luzon Strait, where is a deep basin. The boundary conditions are favorable for solitary IWs to keep the shape unchanged. While 78% of IW packets are concentrated within a range from 116°E to 118°E, where is the transit zone from the deep basin to the continental shelf. The boundary conditions are favorable for solitary IWs originating from the east boundary to fission and evolve into more packets.

[38] The yearly distribution of SAR-observed IW occurrence frequencies from 1995 to 2001 indicates that the occurrence frequencies in 1995, 1998, and 2000 are 2 to 4 times higher than other years. This interannual variability reveals that there are long-term and large-scale processes playing roles in modifying IW occurrence frequency in NSCS. Interannual adjustment of thermocline structures in SCS, as well as the behavior of Kuroshio in the Luzon Strait are accounted such large-scale processes.

[39] The monthly SAR-observed IW occurrence frequencies show that the high occurrence frequencies are distributed from April to July and reach a peak in June with a maximum frequency of 20%. The low occurrence frequencies are distributed in winter from December to February of next year with a minimum frequency of 1.5% in February. Sea surface wind scale statistics and sea state scale statistics indicate that from April to August is a favorable period to IW SAR imaging. These external conditions constitute statistical weights for seasonal distribution of SAR-observed IW occurrence frequencies, but are not thought to be the immediate forcing for IW generation.

[40] For the dynamical analysis of IW generation, this study proposes that the IW generation needs the necessary and sufficient conditions: initial disturbance formation and wave amplitude growth. The tides, tide-topography interaction, west boundary current instability, and others are treated as the necessary conditions for initial disturbance formation, but not the sufficient conditions for IW generation. Owing to dissipation of the initial disturbance, only fully developed waves have a chance to radiate out of the source region. From the physical model, PKdV equation, and solvability conditions, the sufficient conditions for solitary IW growth are derived. The results indicate that the thermocline shoaling provides the forcing to the amplitude growth for westward propagating disturbances, so that the soliton amplitude growth ratio (SAGR), which is parameterized in this study, is a key factor for the variation of the IW occurrence frequency. Theoretical analysis predicts a linear relation between the two. Application of theoretical models to field measurements of ocean upper layer depths determined by the 15°C isotherm and SAR-observed IW occurrence frequency from March to November reveals that the seasonal variability of monthly IW occurrence frequencies result mainly from the seasonal variability of thermocline shoaling. The correlation coefficient is as high as 0.845 with a confidence level of >99%. The linear regression gives a correlation coefficient (R^2) of 0.6519 and a SAGR threshold (minimum) value of 0.90 for IW occurrence. For winter months from December to February of next year, the SAR-observations seem to underestimate the IW occurrence frequencies owing to high occurrence frequencies of unfavorable high sea states, which have highly negative correlation coefficients (-0.823 and -0.844) with the IW occurrence. The eastward propagating initial disturbances have no chance to grow up, therefore, they are hardly observed on the east side of submarine ridge in the eastern Luzon Strait.

[41] **Acknowledgments.** This work was supported by ONR through grants N00014-05-1-0328, N00014-05-1-0606, N00014-04-1-0698, and N00014-05-1-0272, and partially by NASA JPL through subcontract NMO710968. ERS-1/2 and ENVISAT SAR images are copyrighted by ESA. We thank Sonya Legg for help in improving the language of the paper.

References

Boyer, T., and S. Levitus (1994), Quality control and processing of historical oceanographic temperature, salinity, and oxygen data, *NOAA Tech. Rep. NESDIS 81*, pp. 1–64, Natl. Oceanic and Atmos. Admin., Silver Spring, Md.

Cai, S., X. Long, and Z. Gan (2002), A numerical study of the generation and propagation of internal solitary waves in the Luzon Strait, *Oceanol. Acta*, *25*, 51–60.

Djordjevic, V. D., and L. G. Redekopp (1978), The fission and disintegration of internal solitary waves moving over two-dimensional topography, *J. Phys. Oceanogr.*, *8*, 1016–1024.

Ebbesmeyer, C. C., C. A. Coomes, and R. C. Hamilton (1991), New observation on internal wave (soliton) in the South China Sea using acoustic Doppler current profiler, paper presented at Marine Technology Society Conference, Mar. Technol. Soc., New Orleans, La.

Editorial Group of Marine Climate Atlas of Institute of Geography (1982), *Climatic Atlas of Chinese Offshore Areas and Northwest Pacific*, vol. 1, *Wind, Wave and Storm*, pp. 65–115, Press, Beijing.

Guo, B., Z. Huang, P. Li, W. Ji, G. Liu, and J. Xu (2004), *Marine Environment of Offshore and Adjacent Ocean Areas of China*, pp. 189–223, Ocean Press, Beijing.

Ho, C.-R., Q. Zheng, N.-J. Kuo, C.-H. Tsai, and N. E. Huang (2004), Observation of the Kuroshio Intrusion region in the South China Sea from AVHRR data, *Int. J. Remote Sens.*, *25*, 4583–4591.

Hsu, M.-K., and A. K. Liu (2000), Nonlinear internal waves in the South China Sea, *Can. J. Remote Sens.*, *26*, 72–81.

Liu, A. K., Y. S. Chang, M.-K. Hsu, and N. K. Liang (1998), Evolution of nonlinear internal waves in the East and South China Seas, *J. Geophys. Res.*, *103*, 7995–8008.

Liu, A. K., S. R. Ramp, Y. Zhao, and T. Y. Tang (2004), A case study of internal solitary wave propagation during ASIAEX 2001, *IEEE J. Oceanic Eng.*, *29*, 1144–1156.

Meng, J. (2002), *A study of Information Extraction Technology of Ocean Internal Waves From SAR Images*, Ph.D. dissertation, 114 pp., Ocean Univ. of Qingdao, Qingdao, China.

Metzger, E. J., and H. E. Hurlburt (1996), Coupled dynamics of the South China Sea, the Sulu Sea, and the Pacific Ocean, *J. Geophys. Res.*, *101*, 12,331–12,352.

Meyers, G. (1979), Annual variation in the slope of the 14°C isotherm along the equator in the Pacific Ocean, *J. Phys. Oceanogr.*, *9*, 885–891.
Newell, A. C. (1985), *Soliton in Mathematics and Physics*, pp. 1–246, Soc. for Ind. and Appl. Math., Philadelphia, Pa.
Ostrovsky, L. A., and Y. A. Stepanyants (1989), Do internal solitons exist in the ocean, *Rev. Geophys.*, *27*, 293–310.
Phillips, O. M. (1977), *The Dynamics of the Upper Ocean*, 2nd ed., pp. 1–336, Cambridge Univ. Press, New York.
Pohlmann, T. (1987), A three dimensional circulation model of the South China Sea, *Three Dimensional Models of Marine and Estuarine Dynamics*, edited by J. J. Nihoul and B. M. Jamart, pp. 245–268, Elsevier, New York.
Qiao, F., Y. Yuan, Y. Yang, Q. Zheng, C. Xia, and J. Ma (2004), Wave-induced mixing in the upper ocean: Distribution and application to a global ocean model, *Geophys. Res. Lett.*, *31*, L11303, doi:10.1029/2004GL019824.
Shaw, P.-T., and S.-Y. Chao (1994), Surface circulation in the South China Sea, *Deep Sea Res., Part I*, *41*, 1663–1683.
Tappert, F. D., and N. J. Zabusky (1971), Gradient-induced fission of solitons, *Phys. Rev. Lett.*, *27*, 1774–1776.
Wang, B., R. Wu, and R. Lukas (2000), Annual adjustment of the thermocline in tropical Pacific Ocean, *J. Clim.*, *13*, 596–616.
Wang, W., and M. J. McPhaden (2000), The surface layer heat balance in the equatorial Pacific Ocean, Part II: Interannual variability, *J. Phys. Oceanogr.*, *30*, 2989–3008.
Worthington, L. V. (1959), The 18°C water in the Sargasso Sea, *Deep Sea Res.*, *5*, 297–305.
Yuan, Y., Q. Zheng, D. Dai, X. Hu, F. Qiao, and J. Meng (2006), Mechanism of internal waves in the Luzon Strait, *J. Geophys. Res.*, *111*, C11S17, doi:10.1029/2005JC003198.
Zhao, Z. (2004), A study of nonlinear internal waves in the northeastern South China Sea, Ph.D. dissertation, 188 pp., Univ. of Del., Newark.
Zhao, Z., V. Klemas, Q. Zheng, and X.-H. Yan (2004), Remote sensing evidence for baroclinic tide origin of internal solitary waves in the northeastern South China Sea, *Geophys. Res. Lett.*, *31*, L06302, doi:10.1029/2003GL019077.
Zheng, Q., X.-H. Yan, and V. Klemas (1993), Statistical and dynamical analysis of internal waves on the continental shelf of the Middle Atlantic Bight from space shuttle photographs, *J. Geophys. Res.*, *98*, 8495–8504.
Zheng, Q., V. Klemas, and X.-H. Yan (1995), Dynamic interpretation of space shuttle photographs: Deepwater internal waves in the western equatorial Indian Ocean, *J. Geophys. Res.*, *100*, 2579–2589.
Zheng, Q., R. D. Susanto, X.-H. Yan, W. T. Liu, and C.-R. Ho (1998), Observation of equatorial Kelvin solitary wave in the Pacific using TOPEX/Poseidon altimeter data, *Nonlinear Proc. Geophys.*, *5*, 153–165.
Zheng, Q., Y. Yuan, V. Klemas, and X.-H. Yan (2001a), Theoretical expression for an ocean internal soliton SAR image and determination of the soliton characteristic half width, *J. Geophys. Res.*, *106*, 31,415–31,423.
Zheng, Q., V. Klemas, X.-H. Yan, and J. Pan (2001b), Nonlinear evolution of ocean internal solitons as propagating along inhomogeneous thermocline, *J. Geophys. Res.*, *106*, 14,083–14,094.

C.-R. Ho, Department of Marine Environmental Informatics, National Taiwan Ocean University, 2 Pei-Ning Road, Keelung 202, Taiwan. (chungru@sun4.oce.ntou.edu.tw)

Y. T. Song, Jet Propulsion Laboratory, California Institute of Technology, M/S 300-323, 4800 Oak Grove Drive, Pasadena, CA 91109, USA. (song@pacific.jpl.nasa.gov)

R. D. Susanto, Lamont-Doherty Earth Observatory of Columbia University, 61 Route 9W, Palisades, NY 10964, USA. (dwi@ldeo.columbia.edu)

Q. Xu and Q. Zheng, Department of Atmospheric and Oceanic Science, University of Maryland at College Park, 2423 Computer Space Science Building, College Park, MD 20742-2425, USA. (gingxu@atmos.umd.edu; quanan@atmos.umd.edu)